Computational Materials Science 162 (2019) 21–32

Contents lists available at ScienceDirect

Computational Materials Science

journal homepage: www.elsevier.com/locate/commatsci

Phonon spectrum and phonon focusing in coarse-grained atomistic simulations

Yang Li[a,*], Weixuan Li[a], Xiang Chen[a], Adrian Diaz[a], David L. McDowell[b,c], Youping Chen[a]

[a] University of Florida, Department of Mechanical and Aerospace Engineering, Gainesville, FL 32611, USA
[b] Woodruff School of Mechanical Engineering, Georgia Institute of Technology, Atlanta, GA 30332, USA
[c] School of Materials Science and Engineering, Georgia Institute of Technology, Atlanta, GA 30332, USA

ARTICLE INFO

Keywords:
Coarse-grained simulation
CAC
Phonon dispersion relations
Phonon-focusing
Si

ABSTRACT

This work investigates the accuracy, efficiency, and applicability of coarse-grained (CG) atomistic methods in simulation of phonon dynamics. First, we compute and compare phonon dispersion relations in CG models with those in atomically resolved models, using the concurrent atomistic-continuum (CAC). The CG atomistic models using the CAC method are shown to reproduce long-wavelength phonons with great accuracy, while capturing the dynamics of some short-wavelength phonons that are usually inaccessible to CG methods. We then present CG simulation results of the propagation of heat pulses in Si with the interaction between atoms being modelled with the Stillinger-Weber potential; the experimentally observed phonon-focusing patterns in the (1 0 0) and (1 1 1) planes of Si crystals are reproduced. The accuracy and efficiency of the CAC method in CG simulation of acoustic and optical phonon branches are quantified with respect to atomically-resolved molecular dynamics simulations. The applicability and limitations of concurrent multiscale methods in the simulation of phonon transport across atomistic-continuum interface are investigated. Possible ways to overcome the limitations are discussed.

1. Introduction

Advances in time- and space-resolved experimental techniques have created a need for computational methods to simulate phonon thermal transport in complex materials systems at multiple spatial and temporal scales. Such simulations are expected to provide additional insights for interpretation of experimental observations. Although a variety of computational methods have been developed over 30–40 years for simulation of dynamic properties of materials, the classical Molecular Dynamics (MD) method is essentially the only available method that can simultaneously simulate the dynamics of defects and phonons without the need to assume the underlying mechanisms. While MD holds the promise of providing information to understand the dynamic behavior of materials, state-of-the-art supercomputer MD simulations can only practically handle about 10^9 atoms – this limits the number of phonon modes present in the simulation, which is determined by the number of unit cells in the MD simulation cell [1–3], and consequently limits the maximum phonon wavelength. Thus, despite their powerful role in defect dynamics, long-wavelength phonons cannot be captured in a nanoscale MD simulation. Consequently, the need for coarse-grained (CG) methods becomes necessary for simulations of the dynamics of long wavelength phonons and their interactions with defects that have microstructural features beyond the nanoscale.

If we adopt the definition of coarse graining as “the process of representing a system with fewer degrees of freedom than those actually present in the system” [4], many mesoscale or multiscale methods are coarse-grained (CG) methods. Chen et al. [5] divided the CG atomistic methods into three categories: (1) reducing the order of particle representation of molecular structures [6–9], (2) coarse graining the description of the total energy of the system in terms of representative atoms [10–13], and (3) reformulating the field representation of balance laws for multiscale materials description [14–19]. Most of CG models for soft matter that are developed through eliminating fine details of complex molecular structures belong to category (1), while many energy minimization-based CG methods belong to category (2). The formalisms of those methods and the resulting governing equations either substantially alter the dynamics of phonons in the systems or are only suited for equilibrium problems that do not involve the dynamics of waves [20]. By contrast, the CG methods in category (3), e.g., the microcontinuum field theories [21], have been shown to be able to reproduce the dynamics of phonons with a trade-off between accuracy and efficiency [16,22–24].

---

* Corresponding author.
E-mail address: yangli1991@ufl.edu (Y. Li).

https://doi.org/10.1016/j.commatsci.2019.02.020
Received 25 October 2018; Received in revised form 14 February 2019; Accepted 17 February 2019
Available online 26 February 2019
0927-0256/ © 2019 Elsevier B.V. All rights reserved.

The Concurrent Atomistic Continuum (CAC) method is a coarse-grained (CG) atomistic method in the category (3). It coarse grains the description of an atomistic system by reformulating and using the field representation of balance laws. The CAC balance equations were formulated as an extension of the Irving-Kirkwood's statistical mechanical theory of transport processes [25] to a two-level structural description of materials [17,18]. It links and unifies atomistic to continuum descriptions of crystalline materials with the atomic-scale crystal structure and the atomic interactions being built into the formulation. As a result, CAC serves as a tool for CG simulations or concurrent multiscale simulations of material behavior at larger scales [17,18]. The current version of CAC is implemented using the finite element method, with which a material system can be modelled through discretization into finite elements at various resolutions [26]. Although the size of the finite elements can vary from nanometers to microns, domains with different resolutions in the computer model are governed by the same set of conservation laws, with the interatomic potential being the sole supplemental relation. The CAC method aims to complement atomistic methods for the study of dynamic processes at the mesoscale, and it has been demonstrated to be applicable to time-resolved simulations of dislocations [26–31], fracture [32–35], phonon transport [36,37], dislocation-grain boundary interaction [38,39], and phonon-defect interactions [30,40].

The objective of this work is to investigate the accuracy, efficiency, and applicability of CG atomistic method, using CAC as the representative CG tool, in simulation of phonon dynamics. Following the introduction, Section 2 briefly introduces the CAC method; Section 3 outlines the procedures to calculate the phonon dispersion relations for fully atomically resolved models and CG models; Section 4 presents the calculation and simulation results of two specific systems: a one-dimensional diatomic chain described with the Lennard-Jones (LJ) interatomic potential [41] and a three-dimensional Si crystal described with the Stillinger-Weber potential [42]; the computed phonon dispersion relations are interpreted through simulation results of phonon wave packets and heat pulses; the simulation results of phonon-focusing phenomenon are compared with phonon-imaging experiments; the paper ends with a summary and a detailed discussion on possibilities to improve the applicability of CG methods in Section 5.

2. The concurrent atomistic-continuum method

The CAC method is based on a unified atomistic-continuum formulation that links atomistic and continuum descriptions of physical quantities [17,18,43–46]. It reformulates the field representation of conservation laws based on a two-level structural description of crystalline materials using the method of non-equilibrium statistical mechanics. In the CAC description, the lattice deformation is continuous until structural discontinuities are produced by the nucleation of defects, while the atomic deformation relative to the lattice at the subscale is discrete. Through embedding discrete atoms within the lattice points, CAC not only can reproduce acoustic phonons, but also can capture optical phonons in polyatomic crystals, such as Si (a Si primitive unit cell contains two atoms). By contrast, most of existing multiscale methods neglect the internal degrees of freedom within unit cells by considering a bulk unit cell approximation; the displacement field is then homogeneous, which is generally referred to as the Cauchy-Born rule. The lack of the description of relative atomic motion within a lattice cell at the sub-structural level prevents these methods from simulating optical phonons. The CAC balance equation of linear momentum for polyatomic crystalline materials can be written as [26,47]

$$\rho^\alpha \ddot{\boldsymbol{u}}^\alpha + \frac{\gamma^\alpha k_B}{\Delta V}\nabla_{\boldsymbol{x}} T = \boldsymbol{f}_{\text{int}}^\alpha + \boldsymbol{f}_{\text{ext}}^\alpha, \quad \alpha = 1,\ 2,\ \dots \nu, \tag{1}$$

where $\boldsymbol{u}^\alpha = \boldsymbol{u}^\alpha(\boldsymbol{x})$ is the displacement vector of the αth atom in a polyatomic unit cell at point $\boldsymbol{x}$; ν is the number of atoms per unit cell; ΔV is the volume of the primitive unit cell at $\boldsymbol{x}$; $\rho^\alpha = m^\alpha/\Delta V$ is the mass density of the αth atom; k_B is the Boltzmann's constant; $\gamma^\alpha = m^\alpha/\sum_{\alpha=1}^{\nu} m^\alpha$; T is the kinetic temperature; $\boldsymbol{f}_{\text{ext}}^\alpha$ is the external force field; $\boldsymbol{f}_{\text{int}}^\alpha$ is the internal force density, which is a nonlinear, nonlocal function of relative displacements and can be obtained using the interatomic potential for the material system.

For systems with a homogenous temperature field or a uniform temperature gradient, the temperature term in Eq. (1) has the equivalent effect of a surface traction on the boundaries or a body force in the interior of the material [48]. Consequently, Eq. (1) can serve as the governing equations for the material behavior of such systems. As a field equation, Eq. (1) can be discretized at the scale of interest and solved using the finite element method. The atomic displacement field within a finite element (FE) can then be approximated using the finite element shape function $\Phi_\xi(\boldsymbol{x})$ as

$$\boldsymbol{u}_m^\alpha(\boldsymbol{x}) \approx \Phi_\xi(\boldsymbol{x})\boldsymbol{U}_{m\xi}^\alpha, \quad \xi = 1,\ 2,\ \dots N_{npe}, \tag{2}$$

where $\boldsymbol{U}_{m\xi}^\alpha$ is the displacement vector of the αth atom associated with the ξth node of the mth element, and N_{npe} is the number of nodes per element. For a three-dimensional material system, the nodal displacements $\boldsymbol{U}_{m\xi}^\alpha$ is a 3×1 vector. The Galerkin weak form of Eq. (1) can thus be expressed, with the term involving temperature in Eq. (1) being denoted as $\boldsymbol{f}_T^\alpha(\boldsymbol{x})$, as

$$\int_{\Omega(\boldsymbol{x})} \boldsymbol{\Phi}_\eta(\boldsymbol{x})(\rho^\alpha \ddot{\boldsymbol{u}}_m^\alpha(\boldsymbol{x}) + \boldsymbol{f}_T^\alpha(\boldsymbol{x}) - \boldsymbol{f}_{\text{int}}^\alpha(\boldsymbol{x}) - \boldsymbol{f}_{\text{ext}}^\alpha)d\boldsymbol{x} = 0,$$
$$\eta = 1,\ 2,\ \dots N_{npe}. \tag{3}$$

Substituting Eq. (2) into Eq. (3), we have

$$\int_{\Omega(\boldsymbol{x})} \rho^\alpha \Phi_\eta \Phi_\xi \ddot{\boldsymbol{U}}_{m\xi}^\alpha d\boldsymbol{x}$$
$$= \int_{\Omega(\boldsymbol{x})} \Phi_\eta(\boldsymbol{f}_{\text{int}}^\alpha(\boldsymbol{x}) + \boldsymbol{f}_{\text{ext}}^\alpha - \boldsymbol{f}_T^\alpha(\boldsymbol{x}))d\boldsymbol{x}, \tag{4}$$

or in matrix notation as

$$\boldsymbol{M}_{\eta\xi}^\alpha \ddot{\boldsymbol{U}}_{m\xi}^\alpha = \boldsymbol{F}_{m\eta}^\alpha, \tag{5}$$

where

$$\boldsymbol{M}_{\eta\xi}^\alpha = \int_{\Omega(\boldsymbol{x})} \rho^\alpha \Phi_\eta \Phi_\xi d\boldsymbol{x}, \tag{6}$$

$$\boldsymbol{F}_{m\eta}^\alpha = \int_{\Omega(\boldsymbol{x})} \Phi_\eta(\boldsymbol{f}_{\text{int}}^\alpha(\boldsymbol{x}) + \boldsymbol{f}_{\text{ext}}^\alpha - \boldsymbol{f}_T^\alpha(\boldsymbol{x}))d\boldsymbol{x}. \tag{7}$$

Eq. (6) describes a $N_{npe} \times N_{npe}$ mass matrix, while Eq. (7) denotes a force vector. For the sake of computational efficiency, we lump the mass matrix using the row sum method to obtain a diagonal mass matrix for $\eta = 1,\ 2,\ \dots., N_{npe}$, where N_{npe} is the number of nodes per element, as

$$\boldsymbol{M}_\eta^{\alpha(lumped)} = \int_{\Omega(\boldsymbol{x})} \left(\sum_{\xi}^{N_{npe}} \rho^\alpha \Phi_\eta \Phi_\xi \right) d\boldsymbol{x} = \int_{\Omega(\boldsymbol{x})} \rho^\alpha \Phi_\eta d\boldsymbol{x}. \tag{8}$$

Eq. (5) needs to be transformed into the isoparametric space to pursue the solution. The mass and force matrices in the isoparametric space are thus expressed, using $\boldsymbol{J}(\boldsymbol{r})$ to denote the Jacobian, as

$$\boldsymbol{M}_\eta^{\alpha(lumped)} = \int_{\Omega(\boldsymbol{x})} \rho^\alpha \Phi_\eta \boldsymbol{J} d\boldsymbol{r}, \tag{9}$$

$$\boldsymbol{F}_{m\eta}^\alpha = \int_{\Omega(\boldsymbol{r})} \Phi_\eta(\boldsymbol{f}_{\text{int}}^\alpha(\boldsymbol{r}) + \boldsymbol{f}_{\text{ext}}^\alpha - \boldsymbol{f}_T^\alpha(\boldsymbol{r}))\boldsymbol{J} d\boldsymbol{r}. \tag{10}$$

Using Gaussian quadrature to numerically evaluate the integrals, we obtain

$$\boldsymbol{M}_\eta^{\alpha(lumped)} = \int_{\Omega(\boldsymbol{r})} \rho^\alpha \Phi_\eta \boldsymbol{J} d\boldsymbol{r} \approx \sum_{\mu}^{N_{ipe}} w_\mu \Phi_{\eta\mu} \rho^\alpha \Delta V_\mu, \tag{11}$$

$$\boldsymbol{F}_{m\eta}^\alpha = \int_{\Omega(\boldsymbol{r})} \Phi_\eta(\boldsymbol{f}_{\text{int}}^\alpha(\boldsymbol{r}) + \boldsymbol{f}_{\text{ext}}^\alpha - \boldsymbol{f}_T^\alpha(\boldsymbol{r}))\boldsymbol{J} d\boldsymbol{r}$$
$$\approx \sum_{\mu}^{N_{ipe}} w_\mu \Phi_{\eta\mu}(\boldsymbol{f}_{\text{int}}^\alpha + \boldsymbol{f}_{\text{ext}}^\alpha - \boldsymbol{f}_T^\alpha)_{m\mu} \Delta V_\mu, \tag{12}$$

where w_μ is the Gauss quadrature weight of the μth integration point, $\Phi_{\eta\mu}$ is the value of shape function $\Phi_\eta(\boldsymbol{x})$ at the μth integration point, ΔV_μ is the volume of the unit cell at the μth integration point, and N_{ipe} is the number of integration points per element.

After numerical integration, Eq. (4), or equivalently Eq. (5), becomes a set of discretized governing equations with the finite element nodal displacements as the unknowns to be solved. The accuracy, efficiency, and stability of the CAC method are then determined by the two approximations: the displacement approximation (i.e., the shape function) and the numerical integration (i.e., the Gauss quadrature). Simulation results can be post-processed and visualized in terms of finite elements; finite element nodal displacements can also be mapped back into atomic positions to plot the atomic trajectories. Since the only constitutive relation is the nonlocal force-displacement relation, the continuity between elements required in the traditional FE method can be discarded. Consequently, nucleation and propagation of dislocations and/or cracks can be simulated via the sliding and separation between finite elements. Spontaneous nucleation and propagation of defects can thus be simulated without the need of a special numerical treatment or additional constitutive laws. Fig. 1 presents an atomistic model of a crystalline material that is discretized into finite elements with a uniform mesh using the CAC method.

3. Phonon dispersion relations in atomically resolved models and coarse-grained models

3.1. Phonon dispersion relations in atomically resolved models

Experimental techniques, such as neutron scattering, enable one to deduce the phonon dispersion relations of a single crystal, which is the frequency of the normal modes as a function of their wave vectors. To obtain these normal modes of vibration based on the theory of crystal dynamics, i.e., the Born and von Karman theory of crystal dynamics or the dynamic theory of crystals by Born and Huang [49], two approximations are necessarily: (1) the adiabatic approximation to assume that the electrons accommodate themselves rapidly to the changing nuclear coordinates, and (2) the harmonic approximation to ignore higher powers of the nuclear coordinates. With the harmonic approximation, the energy of a crystal in the harmonic approximation can be expressed as,

$$H = \frac{1}{2}\sum_{m} M^\alpha \dot{\boldsymbol{u}}_m^{\alpha\mathrm{T}} \dot{\boldsymbol{u}}_m^\alpha + \frac{1}{2}\sum_{m,n,\alpha,\beta} \boldsymbol{u}_m^{\alpha\mathrm{T}} \boldsymbol{K}_{mn}^{\alpha\beta} \boldsymbol{u}_n^\beta, \quad \alpha,\ \beta = 1, 2, \dots \nu, \tag{13}$$

where M^α is the atomic mass of the αth atom, $\boldsymbol{u}_m^\alpha$ is the displacement vector of the αth atom within the mth unit cell that has position vector $\boldsymbol{R}_m$, $\boldsymbol{K}$ is the stiffness matrix; $\boldsymbol{K}$ can be computed from the second derivative of the potential energy with respect to the separation distance between $\boldsymbol{R}_m$ and $\boldsymbol{R}_n$. Since the total energy is conserved, $dH/dt = 0$, and the equation of motion for the system can then be written as

$$M^\alpha \ddot{\boldsymbol{u}}_m^\alpha = -\sum_{n,\beta} \boldsymbol{K}_{mn}^{\alpha\beta} \boldsymbol{u}_n^\beta. \tag{14}$$

Assuming the general solutions for the displacements of αth atom in the unit cell m as a linear superposition of travelling waves, i.e.,

$$\boldsymbol{u}_m^\alpha = \sum_{\boldsymbol{k}} \tilde{\boldsymbol{u}}_{\boldsymbol{k}}^\alpha \exp(i[\boldsymbol{k}\cdot\boldsymbol{r}_m - \omega_{\boldsymbol{k}} t]), \tag{15}$$

where $\tilde{\boldsymbol{u}}_{\boldsymbol{k}}^\alpha$ is the displacement of the αth atoms for the phonon with wave vector $\boldsymbol{k}$, and $\omega_{\boldsymbol{k}}$ is the angular frequency of the phonon with wave vector $\boldsymbol{k}$. The equations of motion can thus be written as

$$M^\alpha \omega_{\boldsymbol{k}}^2\, \tilde{\boldsymbol{u}}_{\boldsymbol{k}}^\alpha - \sum_{n,\beta} \boldsymbol{K}_{mn}^{\alpha\beta} \exp[i\boldsymbol{k}\cdot(\boldsymbol{r}_n - \boldsymbol{r}_m)]\, \tilde{\boldsymbol{u}}_{\boldsymbol{k}}^\beta = 0, \tag{16}$$

or in matrix form as

$$(\boldsymbol{M}\omega_{\boldsymbol{k}}^2 - \boldsymbol{D})\tilde{\boldsymbol{u}} = 0, \tag{17}$$

where $\mathbf{D}$ is the dynamical $3\nu \times 3\nu$ matrix for each wave vector $\mathbf{k}$. For Eq. (17) to have a nontrivial solution, the determinant of the matrix $(\boldsymbol{M}\omega_{\boldsymbol{k}}^2 - \boldsymbol{D})$ must be zero. The resulting frequency-wave vector $(\omega_{\boldsymbol{k}} \sim \boldsymbol{k})$ relations are called phonon dispersion relations.

The dispersion curves are continuous. However, a finite sized crystal permits only a discrete set of wave vectors, with the number of wave vectors being equal to the number of the primitive unit cells in the crystal. Thus, the number of phonon modes present in an MD simulation is equal to the number of the degrees of freedom (DOFs) of the MD model. Consequently, a finite-sized MD model cannot capture phonons with wavelength longer than the dimensions of the MD simulation cell.

For a 3D crystalline MD model that has N particles, there are $3N$ DOF; this grants 3 N phonon modes with a uniform distribution of 3 N phonon wave vectors over the entire Brillouin-zone. Since the number of phonon modes is determined by the DOFs of the model, the wavelengths of phonons in a crystalline system are consequently limited by the size of the simulation cell; the only exception is the wave vector $\mathbf{k} = 0$, which represents a rigid body motion.

3.2. Phonon dispersion relations in CG models based on the CAC method

The phonon dispersion relations for a CG model can also be calculated using the theory of LD based on the discretized FE equations, e.g., Eq. (5), which describes the motion of FE nodes. In the harmonic approximation, the internal force at an integration point can be expressed as

$$(\boldsymbol{f}_{\mathrm{int}}^\alpha)_{m\mu} = -\textstyle\sum_{n,\xi,\beta} \boldsymbol{K}_{mn\mu\xi}^{\alpha\beta} \boldsymbol{U}_{n\xi}^\beta,$$
$$\alpha,\ \beta = 1, 2, \dots\nu,\ \ \mu = 1,\ 2,\ \dots N_{ipe},\ \xi = 1,\ 2,\ \dots N_{npe}, \tag{18}$$

where $(\boldsymbol{f}_{\mathrm{int}}^\alpha)_{m\mu}$ is the internal force density vector for the αth atom at the μth integration point of the mth element; $\mathbf{K}$ is the tangent stiffness matrix, and $\boldsymbol{U}_{n\xi}^\beta$ is the nodal displacement vector of the βth atom associated with the ξth node of the nth element. In the absence of external force and temperature, Eq. (12) becomes

$$\boldsymbol{F}_{m\eta}^\alpha = -\textstyle\sum_\mu w_\mu \Phi_{\eta\mu} \Delta V_\mu \sum_{n,\xi,\beta} \boldsymbol{K}_{mn\mu\xi}^{\alpha\beta} \boldsymbol{U}_{n\xi}^\beta,$$
$$\mu = 1,\ 2,\ \dots N_{ipe},\ \ \eta = 1,\ 2,\ \dots N_{npe}. \tag{19}$$

Substituting Eq. (19) into Eq. (5), we obtain the equation of motion for the αth atom associated with the ηth node in the mth FE as

$$\left(\sum_\mu w_\mu \Phi_{\eta\mu} \rho^\alpha \Delta V_\mu\right) \ddot{\boldsymbol{U}}_{m\eta}^\alpha = -\sum_\mu w_\mu \Phi_{\eta\mu} \Delta V_\mu \sum_{n,\xi,\beta} \boldsymbol{K}_{mn\mu\xi}^{\alpha\beta} \boldsymbol{U}_{n\xi}^\beta. \tag{20}$$

The periodicity of the finite element mesh then allows us to assume the solution to Eq. (20) in the form of Bloch wave functions, i.e.,

$$\boldsymbol{U}_{m\eta}^\alpha = \sum_{\boldsymbol{k}} \tilde{\boldsymbol{U}}_{\boldsymbol{k}\eta}^\alpha \exp(i[\boldsymbol{k}\cdot\boldsymbol{R}_m - \omega_{\boldsymbol{k}} t]), \tag{21}$$

where $\tilde{\boldsymbol{U}}_{\boldsymbol{k}\eta}^\alpha$ is the polarization vector of the αth atom associated with the

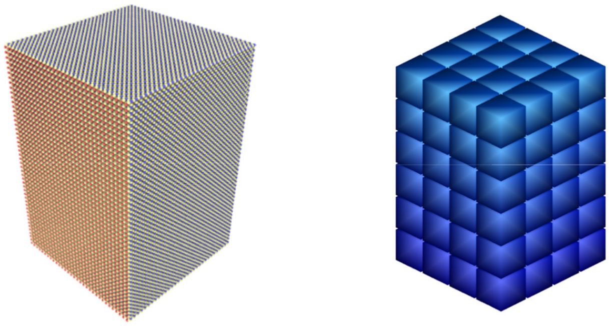

Fig. 1. An atomistic model (left) and a coarse-grained model using the CAC method (right).

ηth node of the mth element for the phonon with wave vector $\mathbf{k}$, and $\boldsymbol{R}_m$ is the position vector of the mth finite element (chosen to be located at the first node of the element for the first atom as a convention), The linearity of Eq. (20) allows us to solve one wave vector $\boldsymbol{k}$ at a time for the phonon mode, i.e.,

$$\left(\sum_\mu w_\mu \Phi_{\eta\mu}\rho^\alpha \Delta V_\mu\right)\omega_{\boldsymbol{k}}^2 \tilde{\boldsymbol{U}}_{\boldsymbol{k}\eta}^\alpha - \sum_\mu w_\mu \Phi_{\eta\mu}\Delta V_\mu \sum_{n,\xi,\beta} \boldsymbol{K}_{mn\mu\xi}^{\alpha\beta}\exp[i\boldsymbol{k}\cdot(\boldsymbol{R}_n - \boldsymbol{R}_m)]\tilde{\boldsymbol{U}}_{\boldsymbol{k}\xi}^\beta = 0, \tag{22}$$

In the matrix notation, this is written as

$$(\boldsymbol{M}\omega_{\boldsymbol{k}}^2 - \boldsymbol{D})\tilde{\boldsymbol{U}} = 0, \tag{23}$$

where $\boldsymbol{D}$ is the dynamic matrix. There are $3N_{npe}\nu$ solutions to Eq. (23), and consequently we have $3N_{npe}\nu$ dispersion curves for a CG model.

4. Numerical results

4.1. Phonon dispersion relations of a one-dimensional diatomic chain

As discussed above, phonon dispersion relations can be calculated using Eq. (17) for a fully atomistic representation and using Eq. (23) for a CG representation. To compare the phonon dispersion relations for a CG model with the underlying atomically resolved model, we first consider a one-dimensional diatomic chain with periodic boundary conditions, as shown in Fig. 2. The interaction between atoms is described by the Lennard-Jones potential [50]. The atoms are separated by 2.56 Å and the lattice constant is $a = 5.12$ Å. The atomic masses of the two types of atoms are 63.55u and 76.26u, respectively, where u is the unified atomic mass unit.

4.1.1. The fully atomically resolved model

For the atomically resolved model, the displacement vectors in Eq. (15) are expressed in terms of the position vectors of the unit cells, and the unit cells can be chosen to have different sizes, the smallest of which is the primitive unit cell. We calculate the phonon dispersion relations of 1D diatomic chain model using a supercell that is 15 times the size of a primitive unit cell (see Fig. 3a), and a supercell that is 5 times the size of a primitive unit cell (see Fig. 3b), respectively, and compare them with the primitive cell representation of the phonon dispersion relations. The displacements in Eq. (15) are thus represented in terms of plane waves defined with two different cell coordinates. As a result of the two different sets of unit cells and lattice vectors, the phonon modes in the same atomistic model are represented by two different sets of wave vectors and wavelengths. The smallest wavelength is 2a for the primitive cell representation of the phonon dispersion relations, while it is 30a (Fig. 3a) and 10a (Fig. 3b) for the supercell representations, resulting in two different representations of the phonon dispersion relations.

It can be seen from Fig. 3, there are two phonon branches in the phonon dispersion relations calculated based on the primitive cell, with the maximum wave vectors being π/a and the minimum wavelength being 2a. By contrast, there are 30 (Fig. 3a) and 10 (Fig. 3b) phonon branches in the supercell representations, with the maximum wave vectors being $\pi/15a$ (Fig. 3a) and $\pi/5a$ (Fig. 3b), respectively, and the minimum wavelength being 30a (Fig. 3a) and 10a (Fig. 3b), respectively. Nevertheless, both primitive cell and supercell representations cover the same range of frequencies and the same number of phonon modes, with the total number of phonon modes being equal to the total number of the DOFs of the system. For the supercells consisting of 15 (or 5) primitive unit cells, the translational symmetry defined by the super cells leads to the folding of the phonon dispersion curves into the supercell Brillouin zone that is 1/15 (or 1/5) of the primitive Brillouin zone of the system [51]. This zone folding gives rise to the additional optical-phonon-like modes. Among the 30 phonon branches in the supercell representation in Fig. 3a, the bottom and top curves represent the same acoustic and optical phonons whose wavelengths are longer than or equal to 30a in the primitive cell representations, the rest of the optical-phonon-like branches represent the acoustic and optical phonons with wavelengths smaller than 30a in the primitive cell representation.

4.1.2. CG models based on the CAC methods

For the CG models, the displacement vectors in Eq. (21) are the FE nodal displacements. For comparison purposes, the finite element size for each CG model is chosen to be the same as that of the supercell, and the calculated phonon dispersion relations are also plotted in Fig. 3. It is seen from Fig. 3 that the FE model shares the same size of the unit cell in the reciprocal space as that of the supercell representation of the atomistic model, and the smallest wavelength is also 30a (Fig. 3a) and 10a (Fig. 3b), respectively.

As can be seen from Fig. 3, CAC reproduces the phonon dispersion curves for acoustic and optical phonons with wavelength longer than 30a (Fig. 3a) and 10a (Fig. 3b), respectively, in good agreement with the atomistic models, except at the Brillouin zone boundaries of the CG models, where phonons have zero group velocity, $\partial\omega/\partial k$, which means that these phonons are standing waves [52].

CAC also reproduces some of the additional optical-phonon-like modes, similar to some of the folded phonon branches in the supercell representations. These additional phonon branches have the same frequencies of the phonons that are represented with wavelengths shorter than 30a in the primitive cell representation. By unfolding the wave vector in the supercell representation into the wave vector in the primitive cell representation [51], we identify these additional optical-phonon-like modes to be the acoustic phonons in the atomically resolved model with primitive unit cell representation that have wavelengths ranging from 2.3a to 2.5a and 7.5a to 10a. This means that some short-wavelength phonons in the primitive cell representation can be well approximated by the FE model.

To investigate the effect of the presence of the additional phonon modes in the CG description, we perform a CAC simulation to pass waves from a fully atomically resolved region to the FE region, using the full interatomic potential. The 1D computer model consists of a coarse-meshed FE region sandwiched between two fully atomically resolved regions, with each element representing 15 primitive unit cells. We then generate a longitudinal acoustic (LA) wave packet with average frequency 5.1 THz, following the procedure outlined by Schelling et al. [53]. The wave packet is centered at wave vector $0.83\pi/a$, corresponding to a phonon mode with wavelength 1.2 nm (=2.4a) in the atomically resolved model with primitive cell representation (marked by a solid black dot in Fig. 3a). The wave packet is allowed to propagate from the atomic region on the left side of the model into the FE region, and then to the atomic region on the right side. Note that the size of the finite elements is 7.7 nm, which is much larger than the phonon wavelength 1.2 nm. Nevertheless, the short-wavelength composition of the wave packet in the atomic region is able to propagate into and transmit across the FE region, as shown in Fig. 4. The energy-transmission coefficient of the wave packet from the atomic region to the FE region is found to be α = 92.5%, while that from the FE region to the atomic region is α = 92.6%. These high energy-transmission coefficients are enabled by the presence of the additional high frequency phonons in the CG representation (marked by an open circle in Fig. 3a) that have matching frequencies with the closely

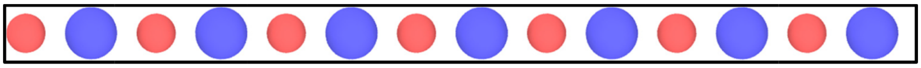

Fig. 2. A one-dimensional diatomic chain with periodic boundary conditions.

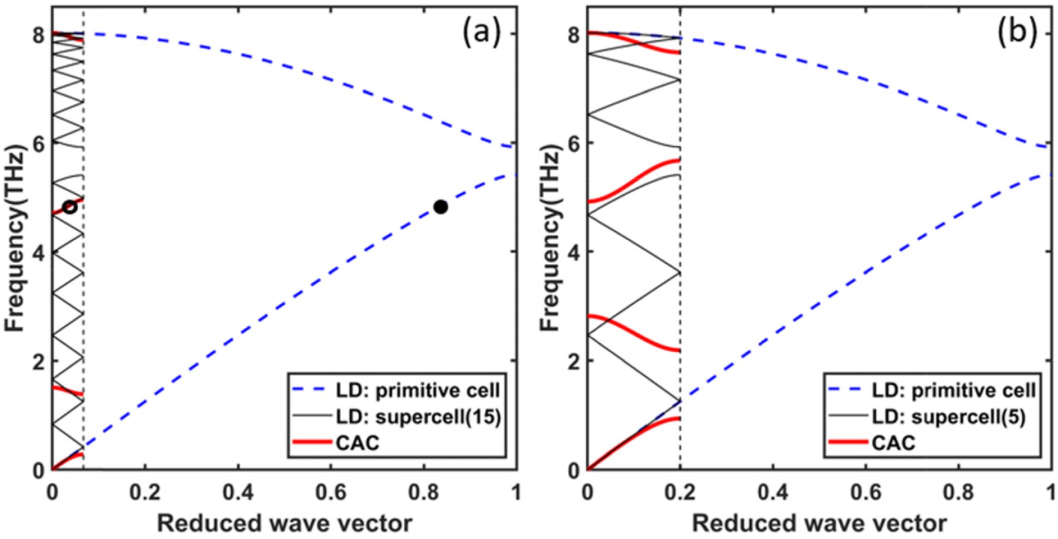

Fig. 3. Phonon dispersion relations of a 1D diatomic chain model calculated with supercells consisting of (a) 15 primitive cells and (b) 5 primitive cells; dashed lines indicate a primitive cell representation, and fine solid lines supercell representation; the results of CG models calculated using CAC are represented by the thick solid lines for comparison. The reduced wave vector is defined as k/k_0 with $k_0 = \pi/a$.

approximated band of short-wavelength phonons in the atomistic representation.

To understand the mechanism by which short-wavelength phonons from an atomically resolved region can propagate across the coarse-meshed finite element region, we perform MD and CG simulation of a one-dimensional diatomic chain with atomic motions associated with the longitudinal phonon mode that has frequency 5.1 THz, respectively. In Fig. 5(a) we present snapshots showing the nodal displacements in the CG model and in Fig. 5(b) the atomic displacements in the MD model. It is seen that the blue atoms associated with the first node of the elements vibrate in exactly the same phase as the corresponding atoms in the MD model. This is because the phonon modes in MD and CG have the same frequency; in addition, the difference between their wave vectors is an integer multiple of reciprocal lattice vector of the system in the supercell representation. The transmission of the short-wavelength phonon in the fully atomically resolved region to the CG region is enabled by the internal atomic motion associated with each finite element node as well as by the discontinuities between finite elements in the CAC method.

4.1.3. *The effect of CG mesh size on the phonon dispersion relations*

To investigate the efficiency and accuracy of CG models with respect to the atomically resolved model, we first construct an MD model that contains 50 unit cells with two atoms situated in each unit cell, as shown in Fig. 2. The number of the DOFs of the MD model is 100 and the length of the model is 25 nm. We then construct three CAC models with length of 25 nm, 100 nm and 500 nm, respectively; each model is discretized with a uniform mesh, having 2, 8 and 40 unit cells in each element, respectively. The three CAC models thus all have the same DOFs as the MD model but different mesh size and specimen length. The results are plotted in Fig. 6 and compared with the analytical LD results for an infinite crystal.

Fig. 6(a) shows that the acoustic and optical phonons present in the MD model have wavelengths ranging from 1 nm (=2a) to 25 nm. Fig. 6(b) shows that the acoustic and optical phonons present in the CAC model with each element containing 2 unit cells covers the same phonon wavelengths as the MD model, the CAC phonon dispersion relations also exactly match the LD results for the same range of phonon wavelengths. This means that the CAC model, if discretized with the finest mesh size, can reproduce the exact phonon dispersion relations computed using MD. However, it is noticed that

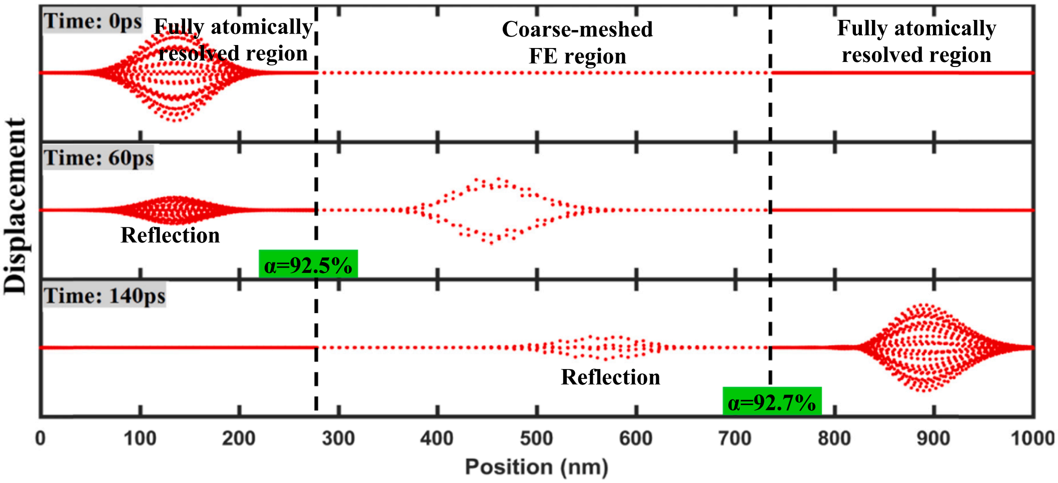

Fig. 4. Snapshots of the displacements during the CAC wave packet simulation of a 1D diatomic chain modelled by two fully atomically resolved regions at the two ends and a CG finite element region in the center of the model; the wave packet is centered at a phonon mode with frequency 5.1 THz and wavelength 1.2 nm (=2.4a). Only the finite element nodes are shown in the CG region.

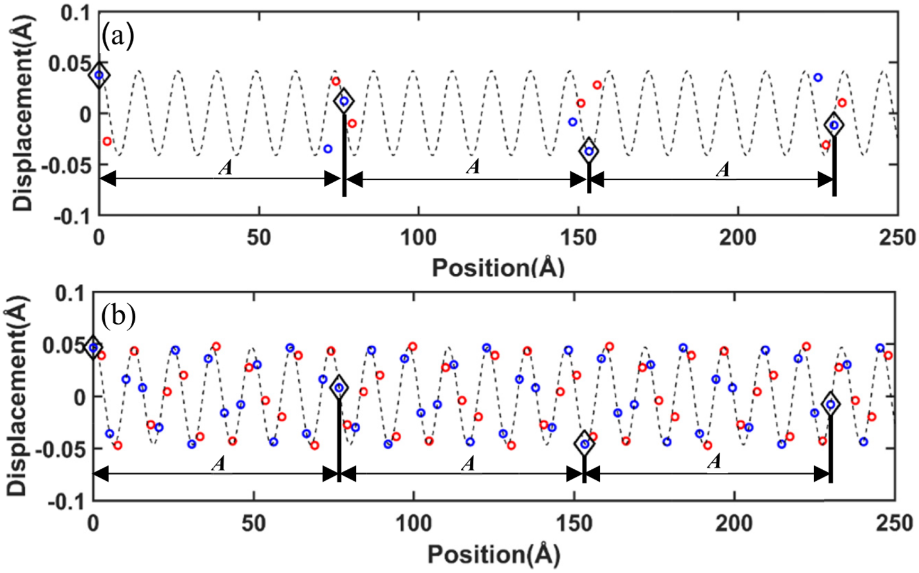

Fig. 5. Snapshots of (a) FE nodal displacements in a CG model, and (b) atomic displacements in a MD model associated with phonons with frequency 5.1 THz, marked in Fig. 3 as open and solid circles, respectively; The blue atoms embedded within the first node of each element and the corresponding atoms in the MD model, are marked by diamonds, showing their identical phases. $A = 15a$ is the separation distance between first nodes of the elements.

the phonons present in the MD model and those in the CAC model with two unit cells per element are limited to wavelengths up to 25 nm.

In Fig. 6(c) and (d) we present the phonon dispersion relations for the CAC models with a larger mesh size. It is seen that the CG computer models can capture the phonons of longer wavelengths of both acoustic and optic branches as the mesh size increases. The range of the wavelength increases linearly with the size of the finite elements as the DOF are held fixed; and the phonon dispersion relations for the long-wavelength phonons compare very well with the LD results for an atomically resolved model. Thus, we can model longer wavelengths while keeping computational expenses bounded.

4.2. Phonon dispersion relations for a three-dimensional Stillinger-Weber Si crystal

4.2.1. Phonon dispersion relations and phonon modes present in a CG model of Si

The second system investigated in this work is a three-dimensional single crystal Si. The Stillinger-Weber potential is used to describe the interaction between Si atoms. The system is modelled using the CAC method and discretized with uniformly meshed rhombohedral-shaped finite elements. The phonon dispersion relations are calculated for an atomically resolved model and then for a CG model with 8 × 8 × 8 unit cells represented per element. The results are plotted in Fig. 7 for wave vectors along the [1 1 1] direction. It is seen from Fig. 7 that the CAC model provides a good description for both acoustic and optical phonons whose wavelengths are larger than $2L$, where $L = 2.35$ nm is the element size, as compared with the LD results. In addition, there are an additional 42 optical-phonon-like modes. They correspond to the folded phonon branches of some of the short-wavelength acoustic and optical phonons present in the atomically resolved model. These additional phonon branches cover a wide range of the frequencies of the short-wavelength phonons represented in the atomically resolved model with the primitive cell representation that have wavelengths shorter than $2L$.

To confirm that these additional phonon modes in the CG description of Si describe the properties of the short-wavelength phonons in the fully atomically resolved model, we build a 3D computer model that

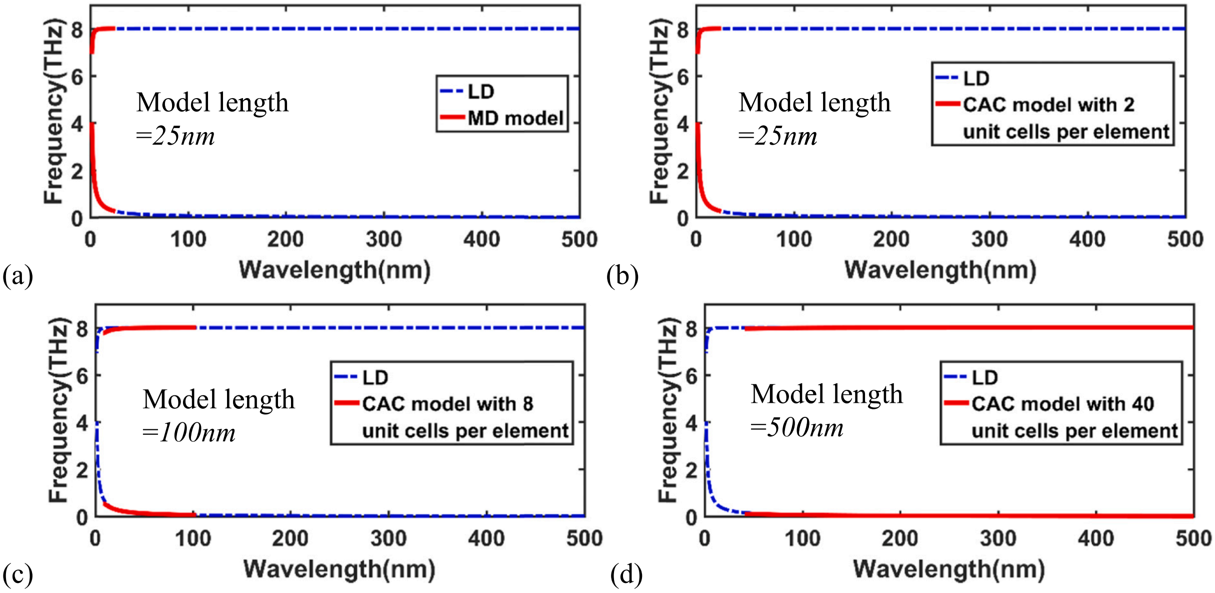

Fig. 6. Phonon dispersion relations, plotted as frequency vs. wavelength, for four different computer models of a diatomic chain with the same number of the DOFs: (a) MD, (b–d) CAC, showing the trade-off between short and long-wavelength phonons simulated in CAC.

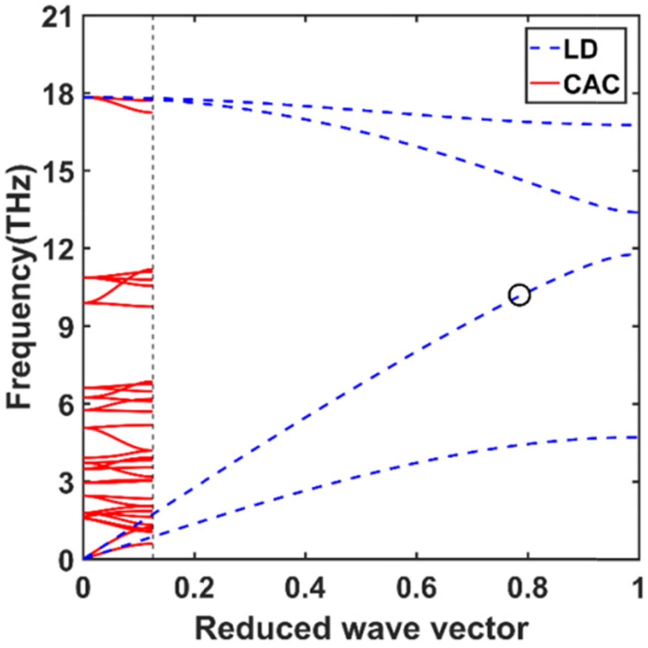

Fig. 7. Phonon dispersion relations for a CAC model of Stillinger-Weber Si with rhombohedral elements along [1 1 1] direction compared with that of LD. Each element contains 8 × 8 × 8 unit cells with each unit cell containing two atoms. Reduce vector is k/k_0, where $k_0 = (0.5,\ 0.5,\ 0.5)2\pi/a_{Si}$, $a_{si} = 5.431$ Å.

consists of both atomically resolved regions and coarsely meshed finite element regions in the [1 1 1] crystallographic direction, in which each finite element represents 512 primitive unit cells. We then perform a wave packet simulation with the wave packet being constructed based on a longitudinal acoustic phonon with frequency 10.2 THz and wavelength 0.8 nm (marked by the circle on the dispersion curves in Fig. 7). The wave packet is allowed to propagate in the [1 1 1] crystallographic direction from the atomic region into the CG region and then to the atomic region on the other side of the model. Snapshots of the atomic displacements in the atomically resolved region and that of the finite element nodal displacements in the CG region during the wave pack propagation are presented in Fig. 8. The energy-transmission coefficient of the wave packet from the atomic to the CG region is found to be 97.1%, while that from the CG to the atomic region is 97.9%. The high energy transmission coefficients again indicate that the CAC method is able to reproduce the behavior of some short-wavelength phonons present in the atomically resolved model.

4.2.2. The effect of CG mesh size on the phonon dispersion relations for long-wavelength phonons

To investigate the effect of mesh size, we compare the phonon dispersion relations for three CG Si models with each linear cubic element containing 2 × 2 × 2, 8 × 8 × 8, 15 × 15 × 15 unit cells, respectively, to the MD and LD results. Each of these CAC models has the same 240 DOFs along the [1 1 1] direction as that of MD. In Fig. 9 we compare the phonon dispersion relations, in terms of wavelength, for the MD model and the CAC models to the analytical LD results.

It is seen from Fig. 9(a) and (b) that the MD model and the CAC model with 2 × 2 × 2 unit cells per element produces the same phonon dispersion relations as that of the LD model for phonons whose wavelength range from 0.6 nm to 37.6 nm. The wavelength range increases as the element size used in the CAC model increases: the CAC model that has elements representing 8 × 8 × 8 unit cells captures phonons with wavelength ranging from 5.0 nm to 150.5 nm, and the CAC model that has elements representing 15 × 15 × 15 unit cells has phonons with wavelength ranging from 9.4 to 282.2 nm. It can be seen in Fig. 9(c) and (d) that the CAC phonons dispersion relations are in good agreement with the LD results for long-wavelength phonons.

4.2.3. Phonon focusing in Si

Phonon focusing is referred to as the phenomenon by which the ballistic heat flux emitted from a point source concentrates along certain directions of the crystal [54–57]. It is an important physical phenomenon in the study of non-equilibrium ballistic phonon propagation. The phenomenon can be understood by considering that the group velocity and wave vector of phonons are not collinear for anisotropic materials, and that a uniform distribution of wave vectors leads to a non-uniform distribution of heat flux [55]; consequently some regions receive very intense energy flux, while others receive very little. Therefore, high energy flux occurs along particular directions. In this section, we examine the accuracy and capability of CAC method in simulating phonon dynamics through reproducing the phonon focusing phenomenon in Si.

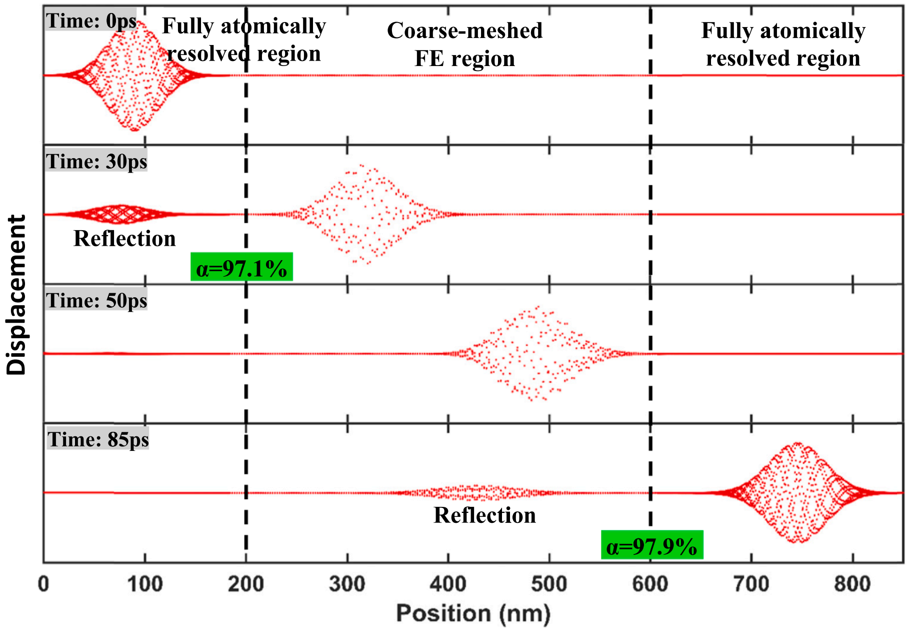

Fig. 8. Snapshots of atomic and nodal displacements during the wave packet simulation of Si for a longitudinal phonon with frequency 10.2 THz and wavelength 0.8 nm. The wave packet propagates from the atomic region on the left side of the model, passing through the CG region, to the atomic region on the right side. The energy-transmission coefficients for the two interfaces are 97.1% and 97.9%, respectively.

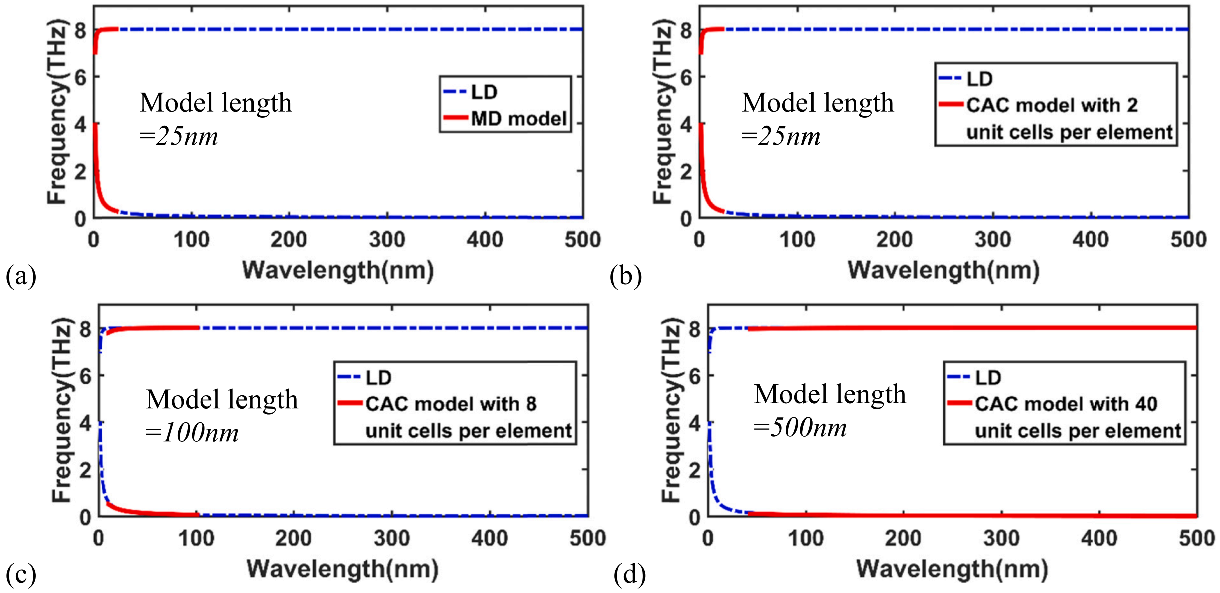

Fig. 9. Phonon dispersion relations for MD and CAC models of the Stillinger-Weber Si along the [1 1 1] direction: (a) MD model, (b–d) CAC models with each linear cubic element containing 2 × 2 × 2, 8 × 8 × 8, 15 × 15 × 15 unit cells, respectively.

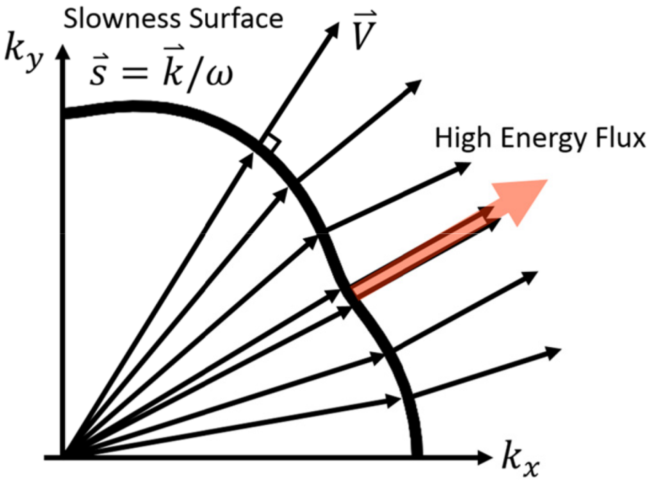

Fig. 10. Geometrical relation between slowness vectors, slowness surface, and group velocity.

The slowness surface is an important tool to study the phonon focusing phenomenon. It is a radial plot of the locus of the slowness vectors for a given frequency and has the shape of the constant-frequency surface in k-space. The slowness vector is defined as $\boldsymbol{s} = \boldsymbol{k}/\omega$, where $\mathbf{k}$ is wave vector, and ω is the phonon frequency. The group velocity vector can be expressed as $\boldsymbol{V} = \partial\omega/\partial\boldsymbol{k}$, which is normal to the constant frequency surface, as shown in Fig. 10. Therefore, when the curvature (Gaussian curvature) of a region at the slowness surface vanishes, it indicates that there are a large number of phonons with the same group velocity along the directions at that region [57]. Correspondingly, large energy flux takes place along these directions [58]. Thus, the properties of phonon focusing in a system can be theoretically predicted according to its slowness surface.

We have presented the phonon dispersion relations for various CAC models in Fig. 9 for Si. The group velocities in each direction can be calculated according to the dispersion relations, which then can be used to find the three-dimensional slowness surface of the CAC model of Si. In Table 1, we present the CAC results of the slow transverse acoustic (STA), the fast transverse acoustic (FTA), and the longitudinal acoustic (LA) slowness surfaces. The slowness surfaces calculated by LD are also presented for comparative purposes. The saddle regions of the slowness surfaces, i.e., the dark shaded regions, are regions where the caustic or high energy flux is supposed to be observed. It is seen from Table 1 that CAC produces slowness surfaces for all the three modes at low frequency in good agreement with LD. It follows from Table 1 that the STA phonons in Si have phonon focusing patterns for (1 1 1) and (1 0 0) surfaces, which indeed have been observed in experiments [59–61].

To reproduce the experimentally observed phenomenon of phonon focusing, we construct two CAC computer models for the visualization of phonon focusing in (1 1 1) and (1 0 0) planes. A 3D Si crystal is discretized with a uniform finite element mesh, with each element contains 8 × 8 × 8 unit cells. The two CAC models have dimensions of 640 × 640 × 16 nm^3 and 860 × 860 × 9 nm^3, respectively; each model contains about 0.3 billion atoms.

Sharp phonon-focusing patterns captured in experiments are mainly attributed to ballistic phonon propagation. High-frequency phonons are susceptible to phonon-phonon scattering; low-frequency acoustic phonons therefore play the major role. In order to reproduce the phonon-focusing phenomenon, in this study a coherent phonon pulse [37,62] with phonons centered at 0.18 THz is applied to mimic the coherent excitation of ballistic non-equilibrium phonons. The coherent phonon pulse is constructed from spatiotemporal Gaussian wave packets by specifying the displacements of atoms in the heat source region according to the phonon dispersion relations.

In Fig. 11(a) and (b) we present the experimentally-imaged phonon focusing patterns [63,64]. In Fig. 11(c) and (d), we present the phonon distribution patterns along [1 1 1] and [1 0 0] orientation on the upper crystal surface obtained from the CAC simulations. The phonon focusing images in the CAC simulation reveal the threefold symmetry in the (1 1 1) surface and twofold symmetry in the (1 0 0) surface of Si; both agree well with the experimental observations. These simulation results demonstrate that the CAC method can provide an accurate description of the non-equilibrium ballistic phonon propagation and is capable of reproducing experimentally-observed phonon focusing phenomena.

Table 1
Three-dimensional STA, FTA, and LA sheets of the slowness surface of CAC model of Si compared with the slowness surface calculated by LD.

	LD slowness surface	CAC slowness surface
3D STA sheet of the slowness surface for Si	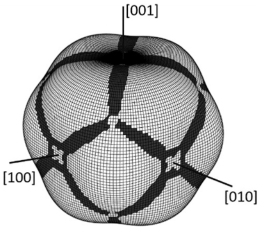	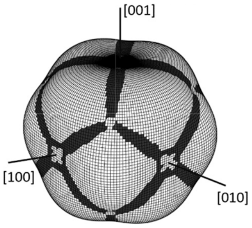
3D FTA sheet of the slowness surface for Si	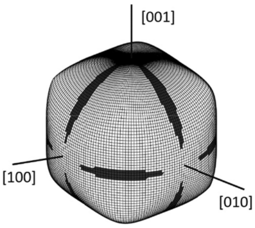	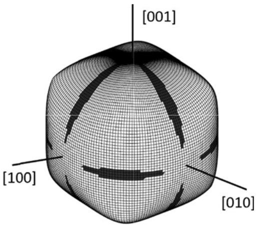
3D LA sheet of the slowness surface for Si	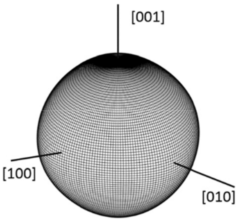	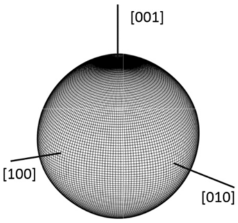

5. Summary and discussion

In this work we have calculated and compared the phonon dispersion relations in coarse-grained (CG) models using the CAC method with that in atomically resolved models for a 1D diatomic chain and a 3D single crystal Si. The CG models are discretized and solved using linear finite elements with a uniform mesh. Major results may be summarized as follows:

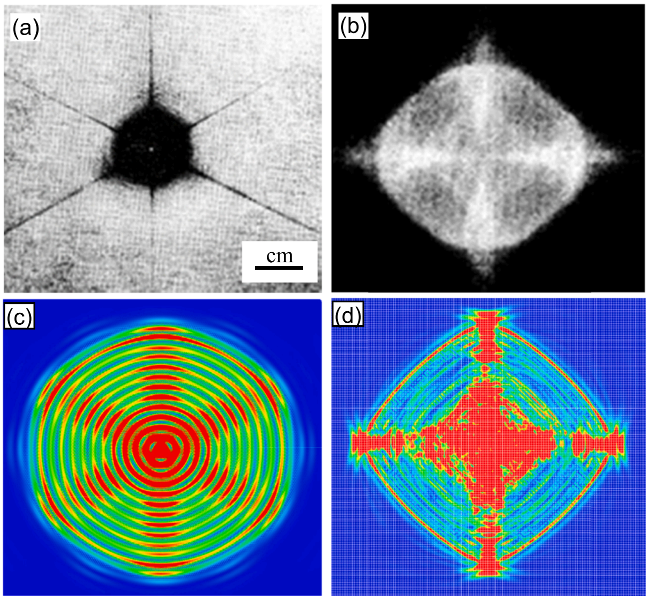

Fig. 11. Phonon focusing patters from phonon-imaging experiments (a) in the (1 1 1) and (b) in the (1 0 0) planes of Si [60,63]; (a) reuses the figure in Kolomenskii and Maznev's paper [63]; (b) reuses the figure in Hauser et al.'s paper [60]. CAC simulation results of phonon focusing (c) in the (1 1 1) and (d) in the (1 0 0) planes of Si.

(1) The CG models using the CAC method have phonon dispersion relations consistent with atomically resolved models for phonons with wavelengths longer than the characteristic length of the element. The longest wavelength phonon that can be present in a CG model increases linearly with the size of the finite elements for a system modelled with the same number of DOF.

(2) The CG models are also shown to be able to capture some phonons whose wavelengths are shorter than the finite element size and are typically unobtainable in other CG approaches. This is confirmed by wave packet simulations showing the propagation of short-wavelength (1.2 nm for the diatomic chain and 0.8 nm for the Si model) phonons from the atomically resolved region to the CG region with a high energy-transmission coefficient, 92.5% for the diatomic chain and 97.1% for the Stillinger-Weber Si. A comparison between the atomic displacements in a MD model and the finite element nodal displacements in a CG model reveals that this is enabled by the internal atomic motion associated with each finite element node and also the non-connectivity between neighboring finite elements.

(3) The phonon-focusing patterns in single crystal Si are reproduced by CAC and are in good agreement with experimental images of phonon focusing in Si. The slowness surfaces of Si calculated using the CAC method are also shown to agree well with those computed via LD.

These results indicate that the CG methods that use a field representation of balance laws, can complement MD for the study of the dynamics of long-wavelength acoustic phonons, e.g., for materials or processes in which long-wavelength phonons interact with defect structures. The accuracy and efficiency of these CG methods are closely related to the shape functions that approximate the displacement field in each element. A special feature of the CAC method is that it can also reproduce optical phonons in addition to some short wavelength phonons determined by the lattice cell size embedded within each finite element node. There are thus possibilities to improve the phonon representation of a CG model using the CAC method. For example, the

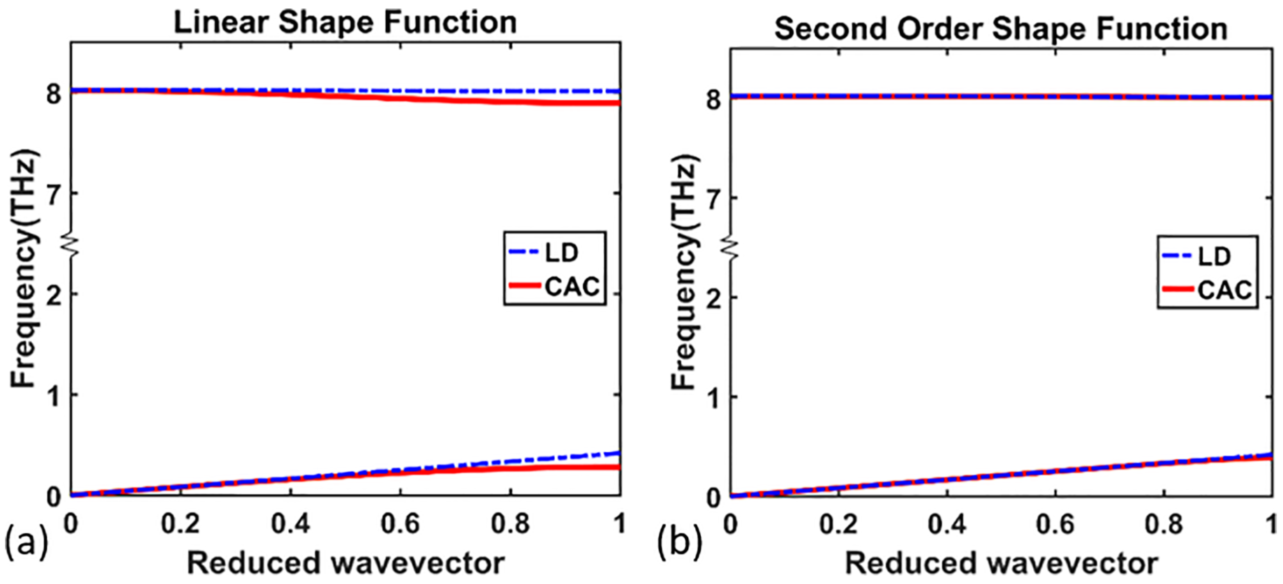

Fig. 12. Frequency-wave vector relations for a 1D diatomic chain using CAC with each element containing 15 unit cells and with (a) a linear shape function and (b) a second-order shape function; the CG relationship is compared with the LD results of the underlying atomically resolved model. Reduced wave vector k/k_0 is used with $k_0 = \pi/15a$.

accuracy of phonon dispersion relations can be increased through higher-order shape functions. Fig. 12 compares the CAC results using a linear shape function with that using a second-order shape function. As can be seen from Fig. 12, the higher order shape function significant increases the accuracy of the CG description.

Another capability of the CAC method is that it can control the description of short-wavelength phonons in the CG region through the subscale structural description in the CAC formulation. As mentioned in Section 2, CAC employs a two-level structural description of the materials, and connectivity between finite elements is not required in the CAC method implemented by the finite element method. Since a unit cell that contains a group of atoms is embedded within each element node, the atomic-scale internal motions associated with a finite element node can be fully described. In addition, relative motions between neighboring nodes of elements are allowed. Consequently, short-wavelength phonons whose wavelengths are smaller than the element size can enter into and propagate in the CG region. Fig. 13 presents snapshots of atomic displacements in a CAC simulation of a 1D diatomic chain. The CAC model is constructed to allow phonons with wavelength around $3a$ (where a is the lattice constant) to present or enter into a CG region. For this purpose, the finite elements are designed to have a unit cell with size $3a$, i.e., containing 6 atoms, embedded within each element node. A phonon wave packet is constructed in the atomic region with average frequency 4.0 THz and wavelength 1.53 nm ($=2.98a$). It is seen from Fig. 13 that the wave packet is able to propagate from the atomic region to the CG region and then to another atomic region. The energy transmission coefficient from the atomic region to the CG region is 97.3% while from the CG region to the atomic region is 96.4%. Similar results are also obtained for a CAC model with unit cells size $4a$ to allow phonons with wavelength around $4a$ to pass from the atomic to the CG region.

This is an interesting feature, as it provides a way to simulate accurately not only the dynamics of long-wavelength phonons but also that of certain desired short-wavelength phonons in the CG region modelled with a uniform FE mesh. Such a feature is especially useful for simulation of phonon transport in materials with disparate length scales, such as polycrystalline materials with micron-sized grains and angstrom-sized GBs. By enabling the passage of short-wavelength phonons from an atomically resolved region of, e.g., a GB, to a coarse-

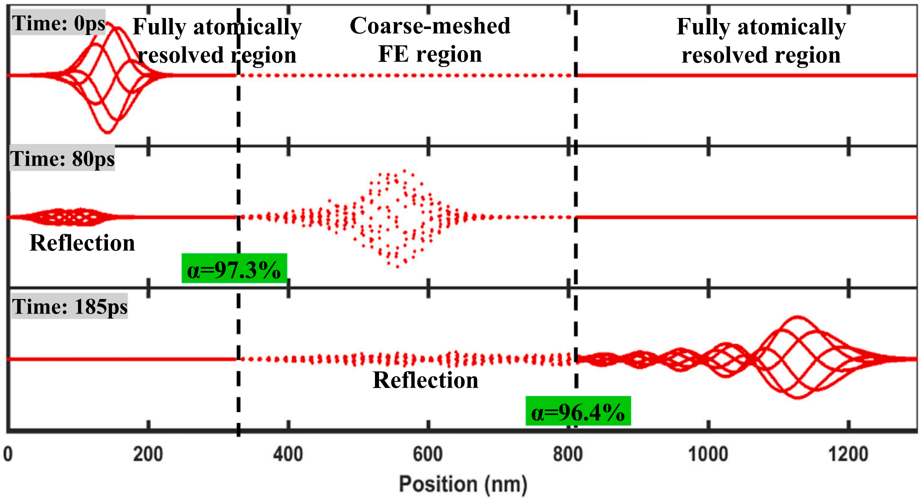

Fig. 13. Snapshots of atomic displacements in the passing wave simulation.

meshed finite element region of single crystalline grain without wave reflections by numerical interfaces, it offers a method to simulate phonon transport at multiple scales. Developing guidelines for such simulations, however, require systematical parametric study; it is thus beyond the scope of this work.

It should be noted that developing concurrent multiscale methods for dynamically coupled mechanical and thermal transport behavior is still a great challenge. The lack of an appropriate phonon representation for the CG continuum region leads to phonon mismatch between atomistic and continuum descriptions. This phonon mismatch leads to the spurious wave reflections at the atomistic-continuum (A–C) interfaces, especially for short-wavelength phonon waves. It is the main obstacle standing in the way of progress of dynamic multiscale methods. Extensive research efforts have been devoted to addressing the problem through minimizing the wave reflection or absorbing heat at the A–C interface. However, it has been suggested that simply minimizing or eliminating the fine scale waves at the A-C interface would further lead to erroneous simulation results, the A–C interface should allow the fine scale waves to pass [65]. Contrary to the extensive existing effects in absorbing waves and heat at the A–C interface, we take a different path to approach this problem by enabling waves to pass the interface. One approach recently proposed to pass short-wavelength phonons from the atomic to the CG finite element region is to use shape functions derived from lattice dynamics to combine linear shape functions and Bloch wave functions [66]. The present work aims to provide a quantitative understanding of the problem of passing waves from the viewpoint of phonon dispersion relations. It is our intent that the results of this work will provide insights into the applicability and limitations of CG methods in the simulation of phonon thermal transport as well as possible ways to overcome the limitations, thereby paving the way to address the key challenge in developing concurrent multiscale dynamic methods so as to enable multiscale simulation of phonon transport in heterogeneous materials.

CRediT authorship contribution statement

Yang Li: Conceptualization, Formal analysis, Methodology, Writing - original draft, Writing - review & editing. **Weixuan Li:** Software, Formal analysis. **Xiang Chen:** Formal analysis, Writing - review & editing. **Adrian Diaz:** Writing - review & editing. **David L. McDowell:** Writing - review & editing. **Youping Chen:** Conceptualization, Writing - original draft, Writing - review & editing.

Acknowledgements

This material is based upon research supported by National Science Foundation with Award numbers CMMI 1761553 and 1761512. The work of Y.L, W.L. and X.C is supported by the U.S. Department of Energy, Office of Science, Basic Energy Sciences under Award # DE-SC0006539. The computer simulations are funded by the Extreme Science and Engineering Discovery Environment (XSEDE) allocations TG-MSS180017 and TG-DMR190008.

Data availability

The raw/processed data required to reproduce these findings cannot be shared at this time due to technical or time limitations.

Appendix A. Supplementary data

Supplementary data to this article can be found online at https://doi.org/10.1016/j.commatsci.2019.02.020.

References

[1] A.J.H. McGaughey, M. Kaviany, Quantitative validation of the Boltzmann transport equation phonon thermal conductivity model under the single-mode relaxation time approximation, Phys. Rev. B 69 (2004) 094303.

[2] D.P. Sellan, E.S. Landry, J.E. Turney, A.J.H. McGaughey, C.H. Amon, Size effects in molecular dynamics thermal conductivity predictions, Phys. Rev. B 81 (2010) 214305.

[3] P.K. Schelling, S.R. Phillpot, P. Keblinski, Comparison of atomic-level simulation methods for computing thermal conductivity, Phys. Rev. B 65 (2002) 144306.

[4] P. Espanol, Novel Methods in Soft Matter Simulations, Springer, 2004, pp. 69–115.

[5] Y. Chen, J. Zimmerman, A. Krivtsov, D.L. McDowell, Assessment of atomistic coarse-graining methods, Int. J. Eng. Sci. 49 (2011) 1337–1349, https://doi.org/10.1016/j.ijengsci.2011.03.018.

[6] S. Izvekov, G.A. Voth, Multiscale coarse graining of liquid-state systems, J. Chem. Phys. 123 (2005) 134105.

[7] S. Izvekov, G.A. Voth, A multiscale coarse-graining method for biomolecular systems, J. Phys. Chem. B 109 (2005) 2469–2473.

[8] W. Noid, et al., The multiscale coarse-graining method. I. A rigorous bridge between atomistic and coarse-grained models, J. Chem. Phys. 128 (2008) 244114.

[9] W. Noid, et al., The multiscale coarse-graining method. II. Numerical implementation for coarse-grained molecular models, J. Chem. Phys. 128 (2008) 244115.

[10] J. Knap, M. Ortiz, An analysis of the quasicontinuum method, J. Mech. Phys. Solids 49 (2001) 1899–1923.

[11] R.E. Rudd, J.Q. Broughton, Coarse-grained molecular dynamics and the atomic limit of finite elements, Phys. Rev. B 58 (1998) R5893.

[12] R.E. Rudd, J.Q. Broughton, Coarse-grained molecular dynamics: nonlinear finite elements and finite temperature, Phys. Rev. B 72 (2005) 144104.

[13] R.E. Rudd, J.Q. Broughton, Concurrent coupling of length scales in solid state systems, Phys. Status Solidi (b) 217 (2000) 251–291.

[14] Y. Chen, J.D. Lee, Connecting molecular dynamics to micromorphic theory. (I). Instantaneous and averaged mechanical variables, Physica A 322 (2003) 359–376.

[15] Y. Chen, J.D. Lee, Connecting molecular dynamics to micromorphic theory. (II). Balance laws, Physica A 322 (2003) 377–392.

[16] Y. Chen, J.D. Lee, A. Eskandarian, Atomistic viewpoint of the applicability of microcontinuum theories, Int. J. Solids Struct. 41 (2004) 2085–2097.

[17] Y. Chen, Reformulation of microscopic balance equations for multiscale materials modeling, J. Chem. Phys. 130 (2009) 134706, , https://doi.org/10.1063/1.3103887.

[18] Y. Chen, J. Lee, Atomistic formulation of a multiscale field theory for nano/micro solids, Philos. Mag. 85 (2005) 4095–4126.

[19] Y. Chen, J. Lee, A. Eskandarian, Atomistic counterpart of micromorphic theory, Acta Mech. 161 (2003) 81–102.

[20] A. Diaz, D. McDowell, Y. Chen, Generalized Models and Non-classical Approaches in Complex Materials, Springer, 2018, pp. 55–77.

[21] A.C. Eringen, Microcontinuum Field Theories: I. Foundations and Solids, Springer Science & Business Media, 2012.

[22] X. Zeng, Y. Chen, J.D. Lee, Determining material constants in nonlocal micromorphic theory through phonon dispersion relations, Int. J. Eng. Sci. 44 (2006) 1334–1345.

[23] Y. Chen, J.D. Lee, A. Eskandarian, Examining the physical foundation of continuum theories from the viewpoint of phonon dispersion relation, Int. J. Eng. Sci. 41 (2003) 61–83.

[24] Y. Chen, J.D. Lee, Determining material constants in micromorphic theory through phonon dispersion relations, Int. J. Eng. Sci. 41 (2003) 871–886.

[25] J. Irving, J.G. Kirkwood, The statistical mechanical theory of transport processes. IV. The equations of hydrodynamics, J. Chem. Phys. 18 (1950) 817–829.

[26] L. Xiong, G. Tucker, D.L. McDowell, Y. Chen, Coarse-grained atomistic simulation of dislocations, J. Mech. Phys. Solids 59 (2011) 160–177.

[27] L. Xiong, Q. Deng, G.J. Tucker, D.L. McDowell, Y. Chen, Coarse-grained atomistic simulations of dislocations in Al, Ni and Cu crystals, Int. J. Plast. 38 (2012) 86–101.

[28] L. Xiong, D.L. McDowell, Y. Chen, Nucleation and growth of dislocation loops in Cu, Al and Si by a concurrent atomistic-continuum method, Scr. Mater. 67 (2012) 633–636.

[29] S. Xu, L. Xiong, Y. Chen, D. McDowell, Validation of the concurrent atomistic-continuum method on screw dislocation/stacking fault interactions, Crystals 7 (2017) 120.

[30] L. Xiong, et al., Coarse-grained elastodynamics of fast moving dislocations, Acta Mater. 104 (2016) 143–155.

[31] L. Xiong, S. Xu, D.L. McDowell, Y. Chen, Concurrent atomistic–continuum simulations of dislocation–void interactions in fcc crystals, Int. J. Plast. 65 (2015) 33–42.

[32] S. Yang, L. Xiong, Q. Deng, Y. Chen, Concurrent atomistic and continuum simulation of strontium titanate, Acta Mater. 61 (2013) 89–102.

[33] Q. Deng, Coarse-graining Atomistic Dynamics of Fracture by Finite Element Method Formulation, Parallelization and Applications, University of Florida, 2011.

[34] Q. Deng, L. Xiong, Y. Chen, Coarse-graining atomistic dynamics of brittle fracture by finite element method, Int. J. Plast. 26 (2010) 1402–1414.

[35] S. Yang, N. Zhang, Y. Chen, Concurrent atomistic–continuum simulation of polycrystalline strontium titanate, Philos. Mag. 95 (2015) 2697–2716.

[36] L. Xiong, X. Chen, N. Zhang, D.L. McDowell, Y. Chen, Prediction of phonon properties of 1D polyatomic systems using concurrent atomistic–continuum simulation, Arch. Appl. Mech 84 (2014) 1665–1675.

[37] X. Chen, A. Chernatynskiy, L. Xiong, Y. Chen, A coherent phonon pulse model for transient phonon thermal transport, Comput. Phys. Commun. 195 (2015) 112–116, https://doi.org/10.1016/j.cpc.2015.05.008.

[38] S. Xu, L. Xiong, Y. Chen, D.L. McDowell, Comparing EAM potentials to model slip transfer of sequential mixed character dislocations across two symmetric tilt grain boundaries in Ni, JOM 1–8 (2017), https://doi.org/10.1007/s11837-017-2302-1.

[39] S. Xu, L. Xiong, Y. Chen, D.L. McDowell, Sequential slip transfer of mixed-character dislocations across Σ3 coherent twin boundary in FCC metals: a concurrent

atomistic-continuum study, NPJ Comput. Mater. 2 (2016) 15016.
[40] X. Chen, L. Xiong, D.L. McDowell, Y. Chen, Effects of phonons on mobility of dislocations and dislocation arrays, Scr. Mater. 137 (2017) 22–26.
[41] M. Kluge, D. Wolf, J. Lutsko, S. Phillpot, Formalism for the calculation of local elastic constants at grain boundaries by means of atomistic simulation, J. Appl. Phys. 67 (1990) 2370–2379.
[42] F.H. Stillinger, T.A. Weber, Computer simulation of local order in condensed phases of silicon, Phys. Rev. B 31 (1985) 5262.
[43] Y. Chen, A. Diaz, Local momentum and heat fluxes in transient transport processes and inhomogeneous systems, Phys. Rev. E 94 (2016) 053309.
[44] Y. Chen, The origin of the distinction between microscopic formulas for stress and Cauchy stress, EPL (Europhys. Lett.) 116 (2016) 34003.
[45] Y. Chen, A. Diaz, Physical foundation and consistent formulation of atomic-level fluxes in transport processes, Phys. Rev. E 98 (2018) 052113.
[46] Y. Chen, Local stress and heat flux in atomistic systems involving three-body forces, J. Chem. Phys. 124 (2006) 054113, , https://doi.org/10.1063/1.2166387.
[47] L. Xiong, Y. Chen, J.D. Lee, Atomistic simulation of mechanical properties of diamond and silicon carbide by a field theory, Modell. Simul. Mater. Sci. Eng. 15 (2007) 535.
[48] L. Xiong, Y. Chen, Coarse-grained simulations of single-crystal silicon, Modell. Simul. Mater. Sci. Eng. 17 (2009) 035002.
[49] M. Born, K. Huang, Dynamical Theory of Crystal Lattices, Clarendon Press, 1954.
[50] P.M. Agrawal, B.M. Rice, D.L. Thompson, Predicting trends in rate parameters for self-diffusion on FCC metal surfaces, Surf. Sci. 515 (2002) 21–35, https://doi.org/10.1016/S0039-6028(02)01916-7.
[51] V. Popescu, A. Zunger, Extracting E versus $\vec{k}$ effective band structure from supercell calculations on alloys and impurities, Phys. Rev. B 85 (2012) 085201.
[52] M.T. Dove, Introduction to Lattice Dynamics vol. 4, Cambridge University Press, 1993.
[53] P.K. Schelling, S.R. Phillpot, P. Keblinski, Phonon wave-packet dynamics at semiconductor interfaces by molecular-dynamics simulation, Appl. Phys. Lett. 80 (2002) 2484–2486, https://doi.org/10.1063/1.1465106.
[54] B. Taylor, H. Maris, C. Elbaum, Phonon focusing in solids, Phys. Rev. Lett. 23 (1969) 416.
[55] B. Taylor, H. Maris, C. Elbaum, Focusing of phonons in crystalline solids due to elastic anisotropy, Phys. Rev. B 3 (1971) 1462.
[56] H.J. Maris, Enhancement of heat pulses in crystals due to elastic anisotropy, J. Acoust. Soc. Am. 50 (1971) 812–818.
[57] W. Eisenmenger, Phonon imaging, J. Phys. Coll. 42 (1981) C6-201–C206-208.
[58] J.P. Wolfe, Imaging Phonons: Acoustic Wave Propagation in Solids, Cambridge University Press, 2005.
[59] R. Wichard, W. Dietsche, Specular phonon reflection: refocusing and symmetry doubling, Phys. Rev. B 45 (1992) 9705.
[60] M.R. Hauser, R. Weaver, J. Wolfe, Internal diffraction of ultrasound in crystals: phonon focusing at long wavelengths, Phys. Rev. Lett. 68 (1992) 2604.
[61] A. Every, W. Sachse, K. Kim, M. Thompson, Phonon focusing and mode-conversion effects in silicon at ultrasonic frequencies, Phys. Rev. Lett. 65 (1990) 1446.
[62] X. Chen, et al., Ballistic-diffusive phonon heat transport across grain boundaries, arXiv (2017).
[63] A.A. Kolomenskii, A.A. Maznev, Phonon-focusing effect with laser-generated ultrasonic surface waves, Phys. Rev. B 48 (1993) 14502–14508.
[64] J.A. Shields, J.P. Wolfe, Measurement of a phonon hot spot in photoexcited Si, Z. Phys. B: Condens. Matter 75 (1989) 11–15.
[65] S.U. Chirputkar, D. Qian, C. Source, Coupled atomistic/continuum simulation based on extended space-time finite element method, Comput. Model. Eng. Sci. 24 (2008) 185.
[66] X. Chen, A. Diaz, L. Xiong, D.L. McDowell, Y. Chen, Passing waves from atomistic to continuum, J. Comput. Phys. 354 (2018) 393–402, https://doi.org/10.1016/j.jcp.2017.10.038.